SCIENTIFIC REPORTS

OPEN

CONFERENCE PROCEEDINGS

APEnergy2014

Single Crystalline Co_3O_4 Nanocrystals Exposed with Different Crystal Planes for Li-O_2 Batteries

Dawei Su[1,2], Shixue Dou[1] & Guoxiu Wang[2]

[1]Institute for Superconducting and Electronic Materials, University of Wollongong, Wollongong, NSW 2522, Australia, [2]Centre for Clean Energy Technology, School of Chemistry and Forensic Science, University of Technology Sydney, Broadway, Sydney, NSW 2007, Australia.

SUBJECT AREAS:
BATTERIES
STRUCTURAL PROPERTIES

Received
27 February 2014

Accepted
9 April 2014

Published
29 August 2014

Correspondence and requests for materials should be addressed to D.W.S. (Dawei@uow.edu.au); S.X.D. (shi@uow.edu.au) or G.X.W. (Guoxiu.Wang@uts.edu.au)

Single crystalline Co_3O_4 nanocrystals exposed with different crystal planes were synthesised, including cubic Co_3O_4 nanocrystals enclosed by {100} crystal planes, pseudo octahedral Co_3O_4 enclosed by {100} and {110} crystal planes, Co_3O_4 nanosheets exposed by {110} crystal planes, hexagonal Co_3O_4 nanoplatelets exposed with {111} crystal planes, and Co_3O_4 nanolaminar exposed with {112} crystal planes. Well single crystalline features of these Co_3O_4 nanocrystals were confirmed by FESEM and HRTEM analyses. The electrochemical performance for Li-O_2 batteries shows that Co_3O_4 nanocrystals can significantly reduce the discharge-charge over-potential via the effect on the oxygen evolution reaction (OER). From the comparison on their catalytic performances, we found that the essential factor to promote the oxygen evolution reactions is the surface crystal planes of Co_3O_4 nanocrystals, namely, crystal planes-dependent process. The correlation between different Co_3O_4 crystal planes and their effect on reducing charge-discharge over-potential was established: {100} < {110} < {112} < {111}.

The high energy density of Li-O_2 battery (2–3 kWh kg^{-1}), which is compatible with gasoline[1,2], is making it to be the most advanced battery system as the power source for electric vehicles (EV). However, it is still far from the demand of realistic application as constrained by several serious issues, like large charge-discharge over-potential and poor cycling stability[3,4]. Previous reports showed non-aqueous rechargeable Li-O_2 batteries only had limited cycles with extremely high charge-discharge voltage gap[5]. The large over-potential during charge-discharge processes is mainly caused by the sluggish oxygen reduction reaction (ORR) and oxygen evolution reaction (OER) of the air cathode. Recently, it was found that the proper non-aqueous electrolyte are the key factors to improve the cycle life of Li-O_2 battery[6–11], and the catalysts have comprehensive benefits on reducing the large charge-discharge voltage gap to increase the electrical energy efficiency for Li-O_2 battery[12–14]. So far, tremendous efforts have been devoted to explore various cathode catalysts, such as metal oxides, metal nitrides and precious metals[15–18]. However, it is still not clear regarding to the theory of catalytic effect of the catalysts on Li-O_2 battery. Therefore, more studies are needed on exploring the essence of catalysts' effect.

The exposed heterogeneous crystal planes of inorganic single crystals play a critical role in determining fascinating surface dependent properties. Essentially, it does not only impact the final shape of the particles themselves, but also generate different effect on their promising applications. Therefore, understanding the nanoscale topography of surface sites, such as terraces, steps, kinks, adatoms and vacancies, and their effects on physicochemical properties is the key to designing nanoscale functional materials by nanotechnology. Follow this strategy, a breakthrough in the synthesis of TiO_2 crystals with 46% high energy {001} facets has been achieved[19], which demonstrated excellent photocatalytic activities. High-index {311} facets Cu_2O microcrystals showing an enhanced specific catalytic rate toward CO oxidation was reported[20]. The crystal-phase and morphology controlled γ-Fe_2O_3 nanomaterials enclosed by the reactive {110} and {100} facets are highly active and distinctively stable for the selective catalytic reduction of NO with NH_3[21].

As one of the commonly available and most studied metal oxides, Co_3O_4, has been widely used in heterogeneous catalysis[22]. The catalytic application is generally facilitated by its high adsorption capacity, high specific area and large part to their surface redox reactivity properties, accordingly, novel Co_3O_4 structures such as nanocubes[23,24], nanorods[25,26], nanowires[27], nanoplatelets[28], nanoboxes[29], and nanodiscs[30], have been synthesized successfully. Even hierarchically flower-like nanomaterials[31], mircospheres[32], and nanoclusters[33], have also been fabricated. Most of the reported Co_3O_4 are enclosed by {001}[34], {110}[22], {111}[35–37], or {112}[30,38,39] facets.

Because the surface energy increases with increasing density of dangling bonds, therefore it is not easy to achieve {*hkl*} on a face-centered cubic (fcc) metal oxide, where {*hkl*} represents high-index planes with at least one Miller index larger than 1[40]. The different crystal planes of Co_3O_4 effect on catalytic property for methane combustion have been reported that follows {112} > {011} ≫ {001} order[38]. It also shows that Co_3O_4 predominantly expose {110} planes not only catalyse CO oxidation at low temperatures but also remain stable in a moist stream of normal feed gas[22].

Herein, the controllable synthesis of Co_3O_4 with different shape and crystal planes and their catalytic properties for Li-O_2 batteries have been systematically studied in this work. Electrochemical performance testing shows Co_3O_4 nanocrystals can significantly reduce the discharge-charge over-potential via the effect on the oxygen evolution reaction (OER). Moreover, it was found that the essential factor to promote the OER is the surface crystal planes of Co_3O_4 nanocrystals, namely, crystal planes-dependent process. The correlation of different Co_3O_4 crystal planes and their effect on reducing charge-discharge over-potential were established: {100} < {110} < {112} < {111}. The study demonstrates that Co_3O_4 based nanomaterials could be applied as effective cathode catalysts for high performance Li-O_2 batteries.

Results and discussion

Phase and crystal structure characterization. Figure 1a shows the FESEM image of CNT. They have approximately 100 nm diameter, as demonstrated by Figure 1b. The size less than 40 nm Co_3O_4 nanocubes were obtained in the solutions containing 10 mL of 0.1 M cobalt nitrate, 5 mL 0.01 M LiOH, and H_2BO_3 via hydrothermal method at 180°C, as observed by FESEM image in Figure 1c and demonstrated by Figure 1d. With concentration of LiOH and H_2BO_3 solution increase, there is edge-truncation along *a* and *b* axes, and the pseudo octahedral Co_3O_4 nanocrystals were achieved, as shown in Figures 1e and f. More FESEM images showing the uniform particle size distribution of Co_3O_4 nanocubes and Co_3O_4 pseudo octahedrons are given in Figures S1 and S2 (Supplementary Information, SI). By comparison, the {110} facets exposed Co_3O_4 nanosheets were synthesised by hydrothermal method also. From the FESEM image and geometric model (Figures 1g and h, Figure S3, SI), it can be seen that they are thin in thickness and have size less than 40 nm.

Two steps method was used to synthesize the {111} facets exposed Co_3O_4 nanoplatelets, following the crystal mismatch guided formation mechanisms. First we designed the precursor exposed with the facets which have the similar atoms arrangement as {111} crystal planes of Co_3O_4. Then, convert the precursor to the targeted product after recrystallization and oxidization at a moderate rate[41]. Therefore, {001} facets exposed $Co(OH)_2$ was chosen as the precursor to obtain {111} facets exposed Co_3O_4 due to the 2% crystal mismatch (atoms arrangement) between them as illustrated by Scheme S1 (SI). Under poly(vinylpyrrolidone) (PVP) surfactant assists, the $Co(OH)_2$ nanoplatelets with hexagonal shape were prepared (Figure S4a, XRD patterns, SI), which have size in the range of 200–300 nm and thickness less than 20 nm (Figure S4b, FESEM image, SI). After sintering, the targeted product, Co_3O_4, preserving the hexagonal platelet shape was obtained, as shown in Figures 1i and j, in which the mesoporous structure can be observed. Because of the gas emission during precursor's thermal decomposition process, it will result in mesoporosity in the final Co_3O_4 nanoplatelets (Figure S5, SI).

Follow the same strategy, the {112} facets exposed Co_3O_4 nanolaminars were converted from $\{02\bar{1}\}$ facets exposed $(NH_4)_2Co_8(CO_3)_6(OH)_6{\cdot}4H_2O$ nanolaminars precursor (Scheme S2, SI). Figures S6 (SI) shows the phase and morphology of $(NH_4)_2Co_8(CO_3)_6(OH)_6{\cdot}4H_2O$ nanolaminars precursor. After sintering, Co_3O_4 nanolaminars with mesoporous structure were obtained, as shown in Figure 1k, and demonstrated by the geometric model (Figure 1l). It can be seen the mesopores distribute uniformly in the Co_3O_4 nanolaminar due to the thermal decomposition of the

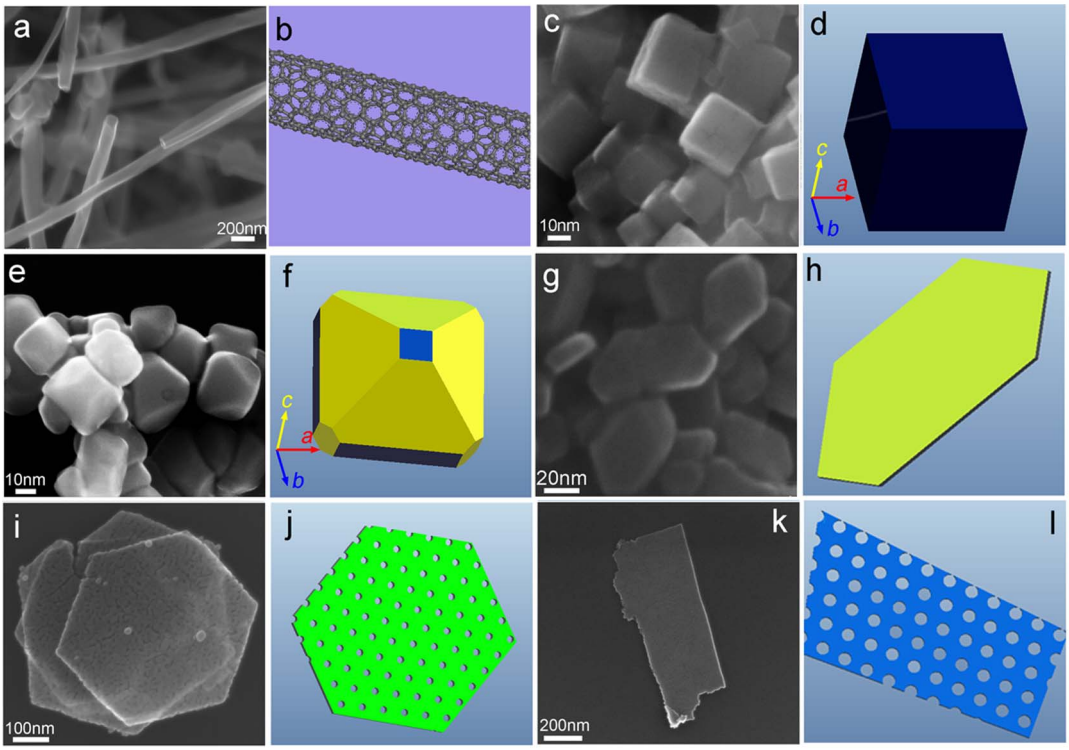

Figure 1 | Morphology characterization of Co_3O_4 nanocrystals exposed with different crystal planes. SEM images and models of CNT (a, b) and Co_3O_4 with different morphologies: nanocubes (c, d), pseudo octahedrons (e, f), nanosheets (g, h), hexagonal nanoplatelets (i, j), and nanolaminar (k, l). Different colours in the models represent different crystal planes: blue: {100}, yellow: {110}, green: {111}, and light blue: {112}.

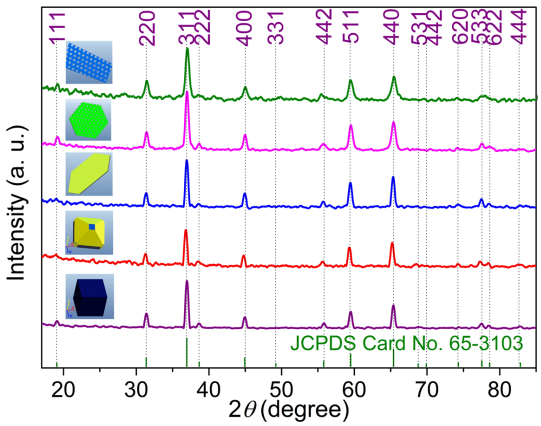

Figure 2 | Phase analysis of Co_3O_4 crystals. XRD patterns of different as-prepared Co_3O_4 nanocrystals.

precursor to release carbonate, hydroxyl groups and ammonium anions. More FESEM images of Co_3O_4 nanolaminar are shown in Figure S7 (SI).

The crystal structures of different as-prepared Co_3O_4 nanocrystals were further confirmed by the X-ray diffraction (XRD) and high resolution transmission electron microscope (HRTEM). In the XRD patterns, as shown in Figure 2, all the diffraction peaks match well with the crystal structure of the spinel Co_3O_4 phase (space group Fd-3m (227)), exhibiting a well-crystalline phase (JCPDS Card No. 65-3103, a = 0.808 nm) without any impurity phase.

Figures 3 a1–a4 shows the HRTEM images of the cubic Co_3O_4 nanocrystals. In Figure 3 a1, the perfect sharp edges, corners and well-defined faces of the Co_3O_4 nanocube can be seen. Figures 3 a2 and a3 show lattice resolved HRTEM image, which is recorded from dotted rectangular area in Figure 3 a1, and corresponding fast-Fourier-transform (FFT) patterns, respectively. The characteristic of square spot array of the FFT pattern suggests that Co_3O_4 nanocubes show single crystal features. All the FFT spots can be indexed

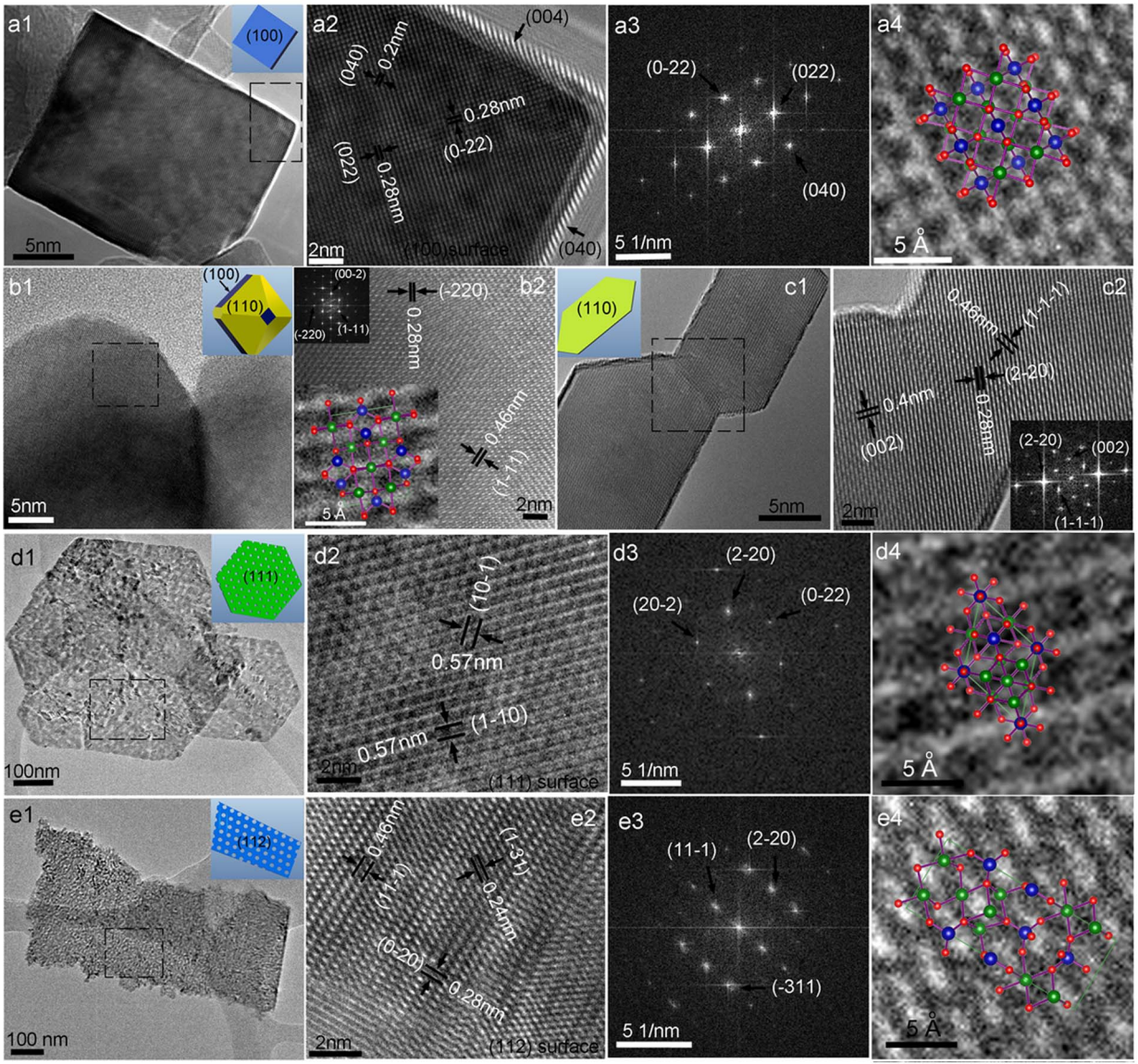

Figure 3 | Structure analysis of Co_3O_4 crystals. HRTEM, fast-Fourier-transform (FFT), lattice and atom resolved HRTEM images of Co_3O_4 nanocrystals exposed with different crystal planes: nanocubes (a1–a4), pseudo octahedrons (b1, b2), nanoplatelets (c1, c2), hexagonal nanosheets (d1–d4) and nanolaminar (e1–e4). Insets in a1, b1, c1, d1, and e1 are corresponding geometric models. Left-top corner inset in b2 and inset in c2 are the corresponding FFT patterns. Insets in a4, d4, and e4 are the crystal structure of {100}, {111}, and {112} crystal planes. Left-bottom inset in b2 is the lattice resolved HRTEM image and corresponding crystal structure of {110} crystal planes.

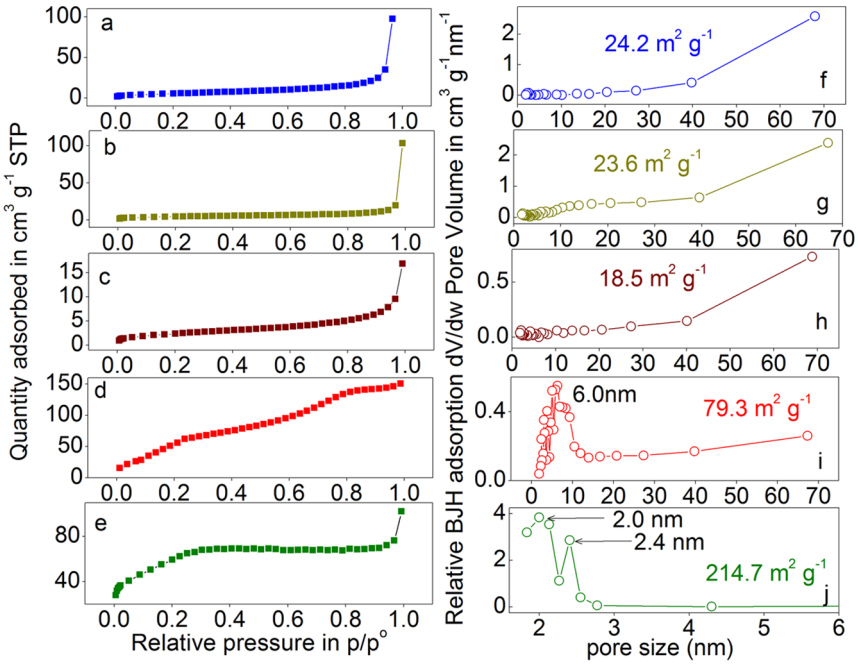

Figure 4 | Surface analysis of Co_3O_4 nanocrystals. N_2 absorption isotherms of (a) Co_3O_4 nanocubes, (b) pseudo octahedral Co_3O_4, (c) {110} facets exposed nanosheets, (d) {111} facets exposed hexagonal nanoplatelets, and (e) {112} facets exposed nanolaminars. (f–j) are their corresponding pore size distribution, derived from absorption hysteresis of Brunauer-Emmett-Teller (BET) surface area measurement. The surface areas are listed in each subfigure from (f) to (j). The average pore sizes of hexagonal Co_3O_4 nanoplatelets and Co_3O_4 nanolaminars are given in (i) and (j).

along [100] zone axis of spinal Co_3O_4 (Figure 3 a3), indicating Co_3O_4 nanocubes are enclosed by {100} facets. The (040) and (022) crystal planes with *d*-spacings of 0.2 and 0.28 nm, respectively, and an interfacial angle of 45° can be directly observed in Figure 3 a2. It is consist with the crystal orientation relationship of spinel Co_3O_4 [100] projected direction. An atom resolved HRTEM image of (100) surface is shown in Figure 3 a4. The inset simulates 4 formula units ($Co^{2+}4Co^{3+}8O16$, 28 atoms in total, the Co^{2+}, Co^{3+}, and O marked as blue, green, and red in colour, respectively) of spinel Co_3O_4 crystal structure along [100] projected direction, from which the Co^{2+} and Co^{3+} ion densities on the surface can be directly calculated. More TEM images of Co_3O_4 nanocubes are given in Figure S8 (SI).

Figure 3 b1 and b2 show TEM images of pseudo octahedral Co_3O_4 nanocrystals. A typical free standing Co_3O_4 octahedron is shown in Figure 3 b1, and its outline and relative enclosed facets is illustrated by the geometric model from the suitable projected direction (inset of Figure 3 b1). In the lattice resolution HRTEM image (Figure 3 b2), two orthogonal crystal planes: $(\bar{2}20)$ and (002), and another crystal plane: $(1\bar{1}1)$ (with 0.46 nm d-spacing, and 144.7 and 54.7° interfacial angles towards $(\bar{2}20)$ and (002) crystal planes, respectively), can be observed. Its corresponding FFT image (inset of Figure 3 b2) shows rhombic spot array, which can be indexed as [110] zone axis. Therefore, the main exposed facets of pseudo octahedral Co_3O_4 nanoparticle should be {110}. More TEM images of pseudo octahedral Co_3O_4 are given in Figure S9 (SI). Figures 3 c1 and c2 show the TEM images of Co_3O_4 nanosheets. From the lattice resolved HRTEM image (Figure 3 c2) and its corresponding FFT pattern image (inset of Figure 3 c2), it can be observed that the dominated facets on both top and down sides of the nanosheets are {110} crystal planes. More TEM images of Co_3O_4 nanosheets are shown in Figure S10 (SI).

The HRTEM images of Co_3O_4 nanoplatelets (Figures 3 d1–d4) prove that they maintain the hexagonal platelet shape of $Co(OH)_2$ precursors (Figure S11, SI), and have mesoporous architecture. It needs to be noticed that although the mesoporous structure is generated, the as-prepared Co_3O_4 nanoplatelets still have single crystalline feature which is consist with the mesocrystal feature[42]. It can be evidenced by the FFT spot patterns, taken from a whole free standing Co_3O_4 nanoplatelet, as shown in Figure 3 d3. All the spots can be well indexed as $(0\bar{2}2)$, $(20\bar{2})$, and $(2\bar{2}0)$ crystal planes along the [111] zone axis. The lattice resolved HRTEM image (Figure 3 d2) shows the $(0\bar{1}1)$, $(10\bar{1})$, and $(1\bar{1}0)$ crystal planes with 0.57 nm *d*-spacing and 60° interfacial angle, which confirm that the Co_3O_4 nanoplatelets are exposed with {111} facets. The rhombic atomic arrangement on the {111} surfaces is shown in the atom resolved HRTEM image (Figure 3 d4) and illustrated by the crystal structure along [111] projected direction (inset of Figure 3 d4).

Figures 3 e1–e4 present the TEM images of Co_3O_4 nanolaminars. In Figures 3 e2 and e3, we can observe $(11\bar{1})$, $(3\bar{1}\bar{1})$, and $(2\bar{2}0)$ crystal planes along the [112] zone axis, which have 0.46, 0.24, and 0.28 nm *d*-spacings, respective. They are less than 2% crystal mismatch with (200), (212), and (012) crystal planes of $(NH_4)_2Co_8(CO_3)_6(OH)_6{\cdot}4H_2O$ precursor. Therefore, it is reasonable to convert the $(02\bar{1})$ facets exposed $(NH_4)_2Co_8(CO_3)_6(OH)_6{\cdot}4H_2O$ nanolaminar precursor into {112} facets exposed Co_3O_4 nanolaminar, maintaining the single crystal feature as illustrated by Scheme S2 (SI). More TEM images of $(NH_4)_2Co_8(CO_3)_6(OH)_6{\cdot}4H_2O$ precursor and Co_3O_4 nanolaminar are given in Figure S12 and Figure S13 (SI), respectively. The {112} crystal planes have more open surface structure than other crystal planes, which can be seen in Figure 3 e4 (the atom resolved HRTEM image and simulated crystal structure along [112] projected direction).

The surface-to-volume ratio and size effects associated with nanoparticles, and surface area information were collected by nitrogen adsorption isotherms at 77 K, as shown in Figure 4. It can be seen the Co_3O_4 nanocubes, pseudo octahedrons, and {110} facets exposed nanosheets show the typical type-II isotherm, which suggests no porous structure in these particles, and they have around 20 m^2 g^{-1} specific BET surface area. While {111} facets exposed hexagonal nanoplatelets, and {112} facets exposed nanolaminars show a typical type-IV isotherm, revealing their mesoporous architecture feature (the average pore size is 6.0 and 2.2 nm respectively (calculated by the Barrett-Joyner-Halenda (BJH) method)). They also have much larger specific BET surface area. To avoid the inconformity affect, the

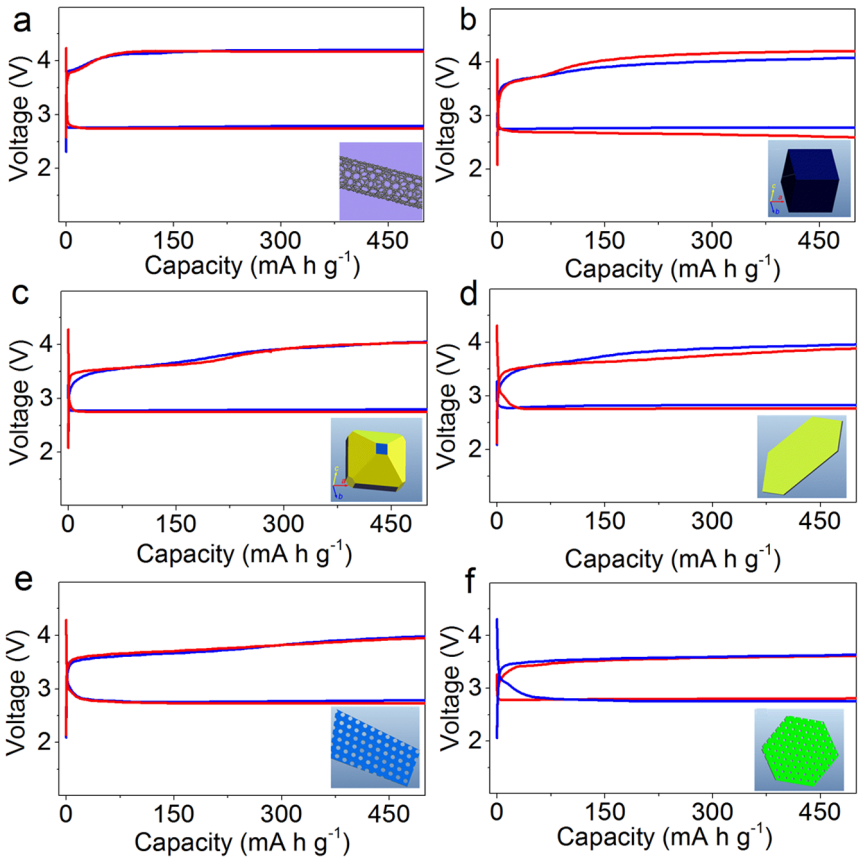

Figure 5 | Electrochemical characterizations at 500 mA h g^{-1} capacity limits. Voltage profiles of (a) bare CNT, and different Co_3O_4 catalysts loaded CNT: (b) Co_3O_4 nanocubes, (c) pseudo octahedral Co_3O_4, (d) {110} facets exposed Co_3O_4 nanosheets, (e) {112} facets exposed Co_3O_4 nanolaminars, and (f) {111} facets exposed hexagonal Co_3O_4 nanoplatelets. Blue and red lines represent the first and second cycles, respectively. Current density is 100 mA g^{-1}.

surface area of different Co_3O_4 samples has been normalized. Figure S14 (SI) shows the adsorption pore area distribution *versus* the pore size of Co_3O_4 nanoplatelets and Co_3O_4 nanolaminars. They have 32.95 and 78.71 m^2 g^{-1} integrated BJH adsorption pore areas, respectively, which were subtracted from the surface areas for the comparison.

Electrochemical performance of single crystalline Co_3O_4 nanocrystals exposed with different crystal planes for Li-O_2 batteries. The electrochemical performance of single crystalline Co_3O_4 nanocrystals exposed with different crystal planes for Li-O_2 batteries was tested through galvanostatical charge and discharge. Figure 5 shows the voltage-capacity profiles of bare CNT and various Co_3O_4 nanocrystal catalysts loaded CNT cathodes with curtailing the capacity to 500 mA h g^{-1}. For the bare CNT electrode, the discharge plateau is at about 2.76 V and the charge plateau is at about 4.2 V during the first and second cycles (Figure 5a). Figures 5b–f demonstrate the charge-discharge profiles of various Co_3O_4 nanocrystal catalysts loaded CNT cathodes. Obviously, they all have lower charge potential by comparison with the bare CNT cathodes. Co_3O_4 nanocubes can achieve the 3.98 V charge potential in the initial cycle, although it was increased to 4.17 V during the second cycle. Pseudo octahedral Co_3O_4 presented the 3.76 V charge plateau on both first and second cycles. {110} facets exposed Co_3O_4 nanoplatelets further got decreased charge potential in the first cycle, which is 3.69 V. {112} facets exposed Co_3O_4 nanolaminars demonstrated about 3.68 V charging potential. {111} facets exposed hexagonal Co_3O_4 nanoplatelets achieved the lowest charge voltage (3.56 V). These observations indicate that Co_3O_4 nanocrystals exposed with different crystal planes have different effect on the catalytic properties for the oxygen evolution reaction (OER), which is lithium peroxides decomposition process.

Specifically, with the normal-spinel structure, Co_3O_4 has two kinds of Co ions: Co^{2+} and Co^{3+}, the Co^{2+} occupies one-eighth of the tetrahedral interstices, while the Co^{3+} ions occupy half of the octahedral interstices as shown in Figure 6a[43,44]. Obviously, the {100}, {110}, {111}, and {112} crystal planes present different atom arrangement, which may result in the different responsible for OER performance. In principle, the nanocrystals' properties are determined by the exposed crystal facets[22,38,45–47]. Metal oxide crystals with particular exposed crystal planes such as high-index facets, could achieve improved chemical or physical performances, because high-index facets have high densities of atom steps, edges, kinks, and dangling bonds, which usually have high chemical activity[48,49]. Furthermore, as confirmed both theoretically[50] and experimentally[37,51], the $Co^{3+}{}_{oct}$ is regarded as the active site compare with the $Co^{2+}{}_{tet}$. Therefore, the $Co^{3+}{}_{oct}$ ion density is the critical factor for their catalytic performance of different surfaces.

The refined crystal structure and relaxed side views of the surface atom configurations of {100}, {110}, {111}, and {112} crystal planes are shown in Figures 6 b–e. The calculated surface energies based on the density function theory (DFT) for Co_3O_4 crystals are listed in Table 1. The {100} crystal plane has the lowest surface energy of 0.92 J m^{-2}, suggesting it is the most stable facet. The {110} crystal planes have the second lowest surface energy (1.31 J m^{-2}). The {112} crystal planes show relatively higher surface energy (1.47 J m^{-2}). The most active crystal planes for Co_3O_4 are the {111} facets, with the

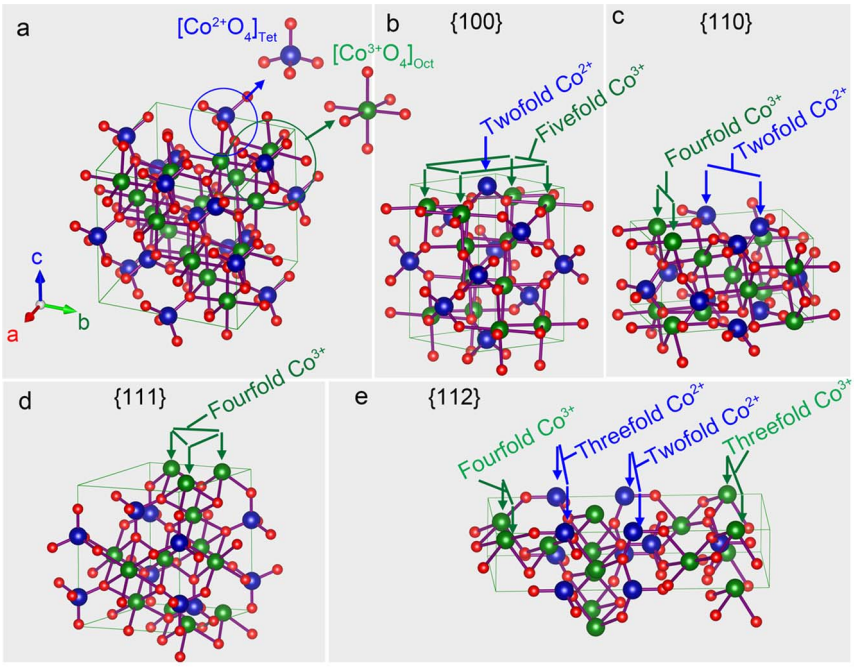

Figure 6 | Crystal structure analysis. Illustration of the cubic Co_3O_4 spinel structure (a), and the atom configurations of the {100} (b), {110} (c), {111} (d), and {112} (e) crystal planes.

highest surface energy of 2.31 J m^{-2}, which is more than two times of {100} crystal planes. Generally, high-energy surfaces have a large density of low-coordinated atoms situated on steps and kinks, with high reactivity[52]. This favours fast ion transfer between the surface and the interior[53,54]. As shown in Table 1, the {111} crystal planes also have the highest dangling bonds density (27.70 $Å^{-2}$, calculated based on the coordinatively unsaturated Co^{2+} and Co^{3+}, as summarized by Table S1, SI), followed by the {112}, {110}, and {100} in order (15.02, 13.02, and 12.27, respectively), which is consisted with their corresponding order on the surface energies ({111} > {112} > {110} > {100}). Interestingly, this tendency is also coordinated with the dangling bonds density of Co^{3+} ions in different crystal planes, as listed by Table 1, confirming the $Co^{3+}{}_{oct}$ is the active site by comparison with $Co^{2+}{}_{tet}$. Therefore, the {111} crystal planes can provide more reactive sites to facilitate OER during the charge process. Similarly, Co_3O_4 nanocubes, pseudo octahedral Co_3O_4, Co_3O_4 nanosheets, and Co_3O_4 nanolaminars presented the gradually improved catalytic performance on OER due to their exposed facets ({100}, {110}, {112}, respectively), which benefited the decrease on the charge potential.

When fully charged and discharged the cells at 200 mA g^{-1} current density, different capacities were obtained in different Co_3O_4 catalysts loaded CNT electrodes, as shown in Figure 7. For the bare CNT electrode (Figure 7a), the initial discharge capacity is about 3000 mA h g^{-1}. After the first cycle, its discharge capacity degraded to 2117 mA h g^{-1}. When electrodes were loaded with Co_3O_4 catalysts, the specific capacity has been significantly improved. As shown in Figure 7b, the CNT with Co_3O_4 nanocubes cathode delivered a specific capacity of 3958 mA h g^{-1} in the first cycle. Although there is decrease on the second cycle, the discharge capacity was still maintained at high value (3746 mA h g^{-1}). Along with the improved catalytic property of different Co_3O_4 nanocrystals, the capacities were increased gradually. With the pseudo octahedral Co_3O_4, {110} facets exposed Co_3O_4 nanosheets, and {112} facets exposed Co_3O_4 nanolaminars, the electrodes can achieve ~4127, 4567, and 4719 mA h g^{-1} discharge capacities, respectively. While the {111} facets exposed hexagonal Co_3O_4 nanoplatelets reached the maximum of 5229 mA h g^{-1} capacity, which is 1.7 times over the bare CNT electrode. The cycling performance of the Co_3O_4 nanoplatelets loaded CNT electrode is shown in Figure S15 (SI). It can be seen that although the discharge capacity decreased upon cycling, the electrode still maintained a discharge capacity of more than 3000 mA h g^{-1}, a high coulombic efficiency of ~95%, and relatively low charge-discharge over-potential within the ten cycle.

By analysing the profiles of discharge and charge curves, we found that the bare CNT electrode delivered an average discharge voltage of 2.7 V and a charge voltage of 4.3 V; while, the Co_3O_4 catalysts added electrodes show much lower charge voltage, especially, the Co_3O_4 nanoplatelets loaded CNT electrode has over-potential of 1.14 V, which is significantly lower than that of the bare CNT electrode (Figure 7f).

Obviously, the improved capacities should be ascribed to the various exposed facets of the as-prepared Co_3O_4 nanocrystals. The cal-

Table 1 | The relaxed surface areas, dangling bonds of Co^{2+} and Co^{3+} ions, and surface energies of {100}, {110}, {111}, and {112} crystal planes

Crystal planes	Relaxed surface area ($Å^2$)	Dangling bonds of Co^{2+} ions number	Dangling bonds of Co^{3+} ions number	Density of dangling bonds of Co^{2+} ions ($Å^{-2}$)	Density of dangling bonds of Co^{3+} ions ($Å^{-2}$)	Total density of dangling bonds ($Å^{-2}$)	Surface energy (J m^{-2})
{100}	34.13	2	2	6.13	6.13	12.27	0.92
{110}	47.96	2	4	4.34	8.68	13.02	1.31
{111}	33.11	0	9	0	27.70	27.70	2.31
{112}	83.23	3	9	3.75	11.26	15.02	1.46

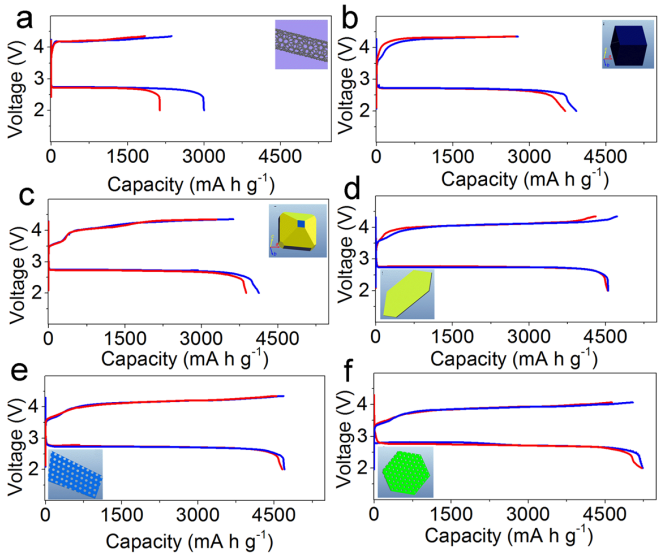

Figure 7 | Electrochemical characterizations. Voltage profiles of (a) bare CNT, and different Co_3O_4 catalysts loaded CNT: (b) Co_3O_4 nanocubes, (c) pseudo octahedral Co_3O_4, (d) {110} facets exposed Co_3O_4 nanosheets, (e) {112} facets exposed Co_3O_4 nanolaminars, and (f) {111} facets exposed hexagonal Co_3O_4 nanoplatelets. Blue and red lines represent the first and second cycles, respectively. Current density is 200 mA g^{-1}.

culated density of states for the {100}, {110}, {111}, and {112} crystal planes with the Li and O atoms present that all of them have the interaction with the Li and O atoms because of the overlapped curves in the density of states (Figure 8). The corresponding electrons density plots (insets of Figure 8) demonstrate the electrons distribution between each crystal plane and the Li and O atoms, confirming different crystal planes of Co_3O_4 could provide reactive sites for the reaction between Li and O atoms. Furthermore, the density of state curves show that {111} crystal planes have the largest interaction with Li and O atoms due to the more overlapped electrons orbits (especially, at the −18.3 eV position), suggesting its highest catalytic property for the Li and O reaction.

Conclusion

In summary, single crystalline Co_3O_4 nanocrystals exposed with different crystal planes were synthesised, including nanocubes, pseudo octahedrons, nanosheets, hexagonal nanoplatelets and nanolaminar. As confirmed by FESEM and HRTEM analyses, they are exposed with {100}, {110}, {111}, and {112} crystal planes, respectively. The electrochemical performance for Li-O_2 batteries shows that Co_3O_4 nanocrystals can significantly reduce the discharge-charge over-potential via the effect on the oxygen evolution reaction (OER), and achieve high specific capacity, leading to a high round-trip efficiency. From the comparison of the catalytic performance of different Co_3O_4 nanocrystals, it knows that the essential factor to promote the OER of Co_3O_4 nanocrystals is the surface crystal planes. The correlation of different Co_3O_4 crystal planes and their effect on reducing charge and discharge over potential was established: {100} < {110} < {112} < {111}, which were verified by theoretical calculations and experiments analyses. The study demonstrates that Co_3O_4 based nanomaterials could be applied as effective cathode catalysts for high performance Li-O_2 batteries.

Methods

Synthesis. All chemicals were analytical grade and were used as received without further purification. And all chemicals were supplied by Sigma-Aldrich. $Co(NO_3)_2{\cdot}6H_2O$, $LiOH{\cdot}H_2O$, H_2BO_3, poly(vinylpyrrolidone) (PVP), NaOH, urea ($CO(NH_2)_2$), cationic surfactant cetyltrimethylammonium bromide (CTAB), H_2O_2, and KOH all have the high purity (≥97%). The multiwall carbon nanotubes were purchased from Sigma-Aldrich.

Co_3O_4 nanocube and Co_3O_4 pseudo octahedrons. Their synthesis followed the PH-control strategy. In a typical synthesis, 1 mmol $Co(NO_3)_2{\cdot}6H_2O$ were dissolved in a 10 mL distilled water, than 5 mL 0.01 M $LiOH{\cdot}H_2O$, and H_2BO_3 solution was added. After 20 mins magnetic stirring, the mixture was transfer into a Teflon-lined autoclave (25 mL in capability) sealed by the stainless steel jar. The autoclave was heated to 180°C and maintained at that temperature for 12 h. After cooling to room temperature, the Co_3O_4 nanocubes were collected by centrifugation and washed thoroughly with distilled water several times. To synthesize Co_3O_4 pseudo octahedrons, the same procedure was followed, but with manipulation of the concentration of $LiOH{\cdot}H_2O$ and H_2BO_3: 5 mL of 0.1 M LiOH and H_2BO_3 solution were dissolved in the 10 mL of 0.1 M $Co(NO_3)_2{\cdot}6H_2O$.

{110} facets exposed Co_3O_4 single crystal nanosheet. It was synthesized by a redox-precipitation route as follows: 5 mL of 30 wt.% H_2O_2 aqueous solution was added into 10 mL of a 0.02 M $Co(NO_3)_2{\cdot}6H_2O$ aqueous solution under vigorous stirring. The pH of the solution was adjusted by the addition of a 2 M KOH solution to reach 8.0 slowly (be careful, during this process a vigorous reaction was happened). After that, the mixed solution was then transferred into 25 mL Teflon-lined autoclave and heated to and maintained at 180°C for 16 h. The autoclave was cooled naturally to room temperature. Co_3O_4 single crystal nanosheets were obtained by filtration, several washing steps with distilled water and ethanol, and drying at 60°C for 12 h.

Hexagonal Co_3O_4 nanoplatelets. Follow the crystal mismatch guided formation mechanism, $Co(OH)_2$ as precursor were prepared by the precipitation and hydrothermal process first. In a typical procedure, 1.2 g of $Co(NO_3)_2{\cdot}6H_2O$ were dissolved in a 10 mL mixture of ethanol and distilled water with a 1 : 1 volume. As a surfactant, 1 g of poly(vinylpyrrolidone) (PVP) were added. After 30 mins magnetic stirring, 25 mL of a 0.4 M NaOH aqueous solution was slowly added, taking 1.5 h accompany with the colour evolution from blue to red-pink, indicating the phase change from the α to β phase of $Co(OH)_2$. Then the reaction suspension was quickly transferred into a Teflon-lined autoclave. The autoclave was heated to 120°C and maintained at that temperature for 10 h. After cooling to room temperature, the pink product was collected by centrifugation and washed thoroughly with distilled water several times. The β-$Co(OH)_2$ precursors were obtained after drying for 12 h at 60°C in the vacuum oven. The final mesoporous Co_3O_4 nanocrystals were prepared by annealing β-$Co(OH)_2$ precursor at 450°C for 2 h in the tube furnace under atmospheric environment with a slow heating rate (2.0°C min^{-1}).

{112} facets exposed Co_3O_4 nanolaminars[55]. Similarly, follow the crystal mismatch guided formation mechanism, Co_3O_4 nanolaminars enclosed by {112} facets were obtained converting from the $(NH_4)_2Co_8(CO_3)_6(OH)_6{\cdot}4H_2O$ nanolaminars single crystals precursor synthesised by the hydrothermal condition. In a typical procedure, 1 mmol $Co(NO_3)_2{\cdot}6H_2O$, 4 mmol urea ($CO(NH_2)_2$), and 0.2 g cationic surfactant cetyltrimethylammonium bromide (CTAB) as soft template were dissolved in distilled water (20 mL) at room temperature. The mixture was stirred vigorously for several mins until a transparent red solution was formed, and then transferred into the Teflon-lined autoclave (25 mL in capability). After heating and maintaining at 140°C for 12 h, the precipitate was cooled down to room temperature naturally, collected and washed with distilled water and ethanol several times. The final product Co_3O_4 nanolaminars, were obtained by thermal treatment of the above precursors at 450°C for 2 h in the tube furnace under atmospheric environment with a slow heating rate (2.0°C min^{-1}).

Structural and physical characterization. The phase and crystallographic structure of as-prepared Co_3O_4 nanocrystals were characterized by powder X-ray diffraction (XRD) using a Siemens D5000 diffractometer equipped by a Cu Kα1 radiation (λ = 1.54056 Å) with 2θ ranging from 15° to 85° at a scanning step of 0.02° sec^{-1}. The size and morphology was analysed by high resolution field emission scanning electron microscopes (FESEM) Zeiss Supra 55VP. The microscope was operated at a working distance of 2 mm with an acceleration voltage of 10 kV and an in-lens detector was used for the imaging. The crystal structural details were further characterized by high-resolution transmission electron microscopy (HRTEM) FEGTEM 3000 (JEOL 300 KV Atomic Resolution Transmission Electron Microscope (0.192 nm resolution)) worked at an accelerating voltage of 300 kV. The bright field image (BF) and selected area electron diffraction (SAED) patterns were recorded by a Gatan CCD camera in a digital format. The surface area information was collected by N_2 adsorption isotherm using a Quadrasorb SI analyzer at 77 K. Brunauer–Emmett–Teller (BET) surface areas were calculated using experimental points at a relative pressure of P/P_0 = 0.05–0.25. The pore size distribution was calculated by the Barret–Joyner–Halenda (BJH) method.

Electrochemical testing. A Swagelog-type cell was designed to investigate the charge and discharge properties and cyclability in Li-O_2 batteries, which consisted of a stainless steel cylinder plunger to support a Li foil anode (3 mm × ø 15 mm) and a special stainless steel tube to allow oxygen access to the back side of the cathode. The oxygen electrodes were prepared as follows: catalyst slurry was-prepared by mixing the as-prepared catalysts (90 wt. %) with poly(tetrafluoroethylene) (PTFE) (10 wt. %) in isopropanol. The mixture was then coated on a glass fibre separator. The

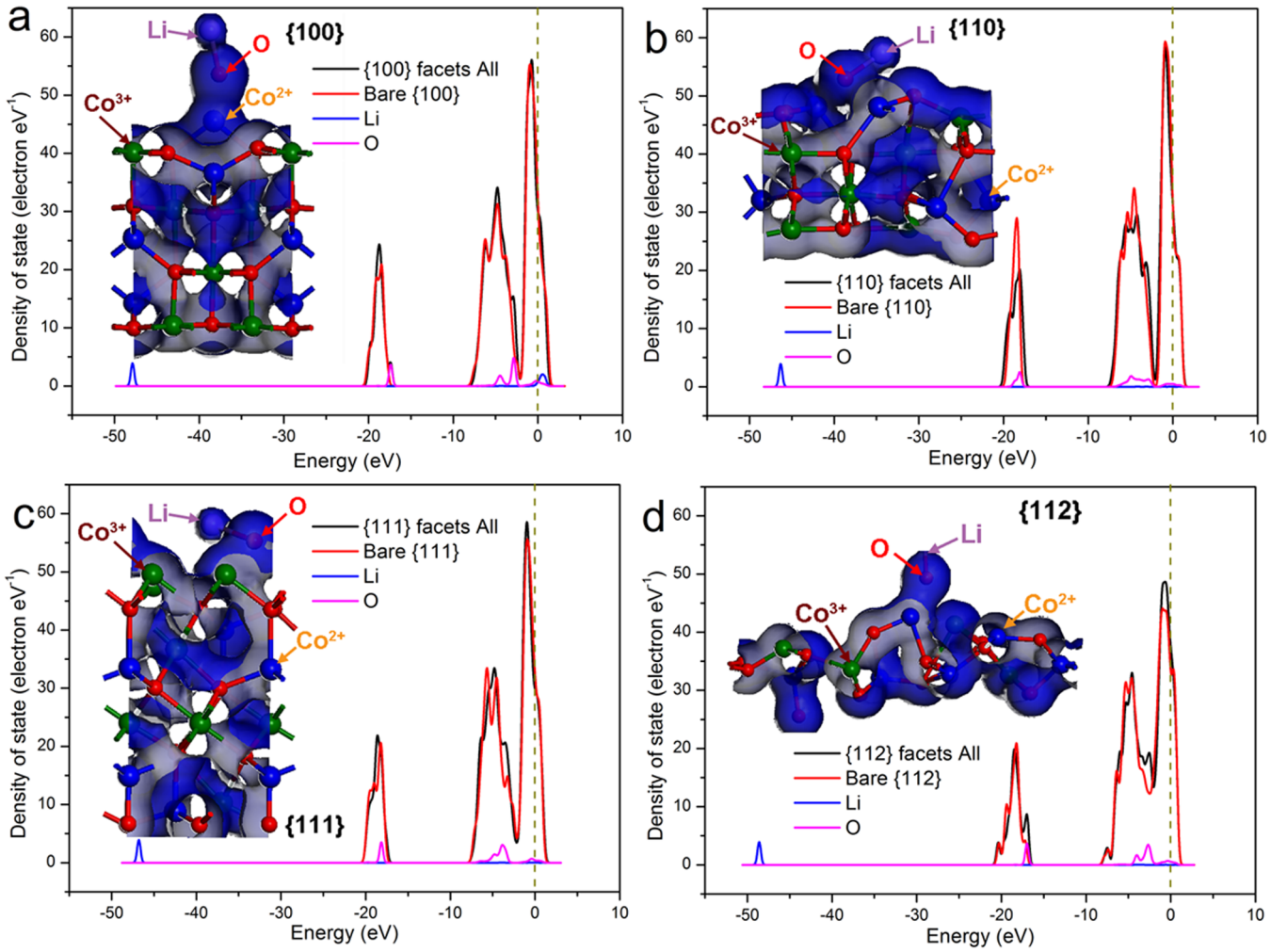

Figure 8 | Electrons density analysis. Density of state for the {100} (a), {110} (b), {111} (c), and {112} (d) crystal planes interacting with the Li and O atoms. Insets of each subfigure are the corresponding electrons density plots.

cathode film was punched into discs with a diameter of 14 mm and dried at 110°C in a vacuum oven for 12 h. The typical loading of the air electrode is about 1 mg carbon cm^{-2}. The cathode was placed onto the separator and a thin open 316 stainless steel mesh was placed on top to act as a current collector. The entire cell was gastight except for the stainless steel mesh window exposed the porous cathode to the O_2 atmosphere. The Li-O_2 cells were assembled in an Ar filled glove box (Unilab, MBRAUN, Germany) with water and oxygen level less than 0.1 ppm. A glass microfiber filter (Whatman, ø 21 mm) separator will be used, soaked in 1 M $LiNO_3$ (99.99%, Sigma-Aldrich) in dimethyl sulfoxide (DMSO, anhydrous, >99.9%, Sigma-Aldrich) electrolyte. The cell was gas-tight except for the stainless steel mesh window that exposed the porous cathode film to the oxygen atmosphere. All measurements were conducted in 1 atm dry oxygen atmosphere to avoid any negative effects of humidity and CO_2. Galvanostatic discharge charge was conducted on a Neware battery testing system. Because the as-prepared Co_3O_4 nanocrystals present different surface areas, to avoid the inconformity affect, when the electrodes were prepared, the surface area of different Co_3O_4 samples has been normalized, which means the different mass of different Co_3O_4 nanocrytals were added into the CNT to keep that the total exposed crystal planes of different Co_3O_4 nanocrystals have the same area. Especially, for the {111} facets exposed hexagonal Co_3O_4 nanoplatelets and {112} facets exposed Co_3O_4 nanolaminars, because they show mesoporous architecture feature, the pore areas of them were subtracted from the surface areas. The specific capacity was calculated based on the mass of CNT in the cathode electrodes.

Computational methods. The calculations were performed based on the density-functional theory (DFT) approach[56] with the ABINIT[57,58]. The exchange-correlation energy function was represented by the local-density approximation (LDA) employing ultra-soft pseudopotential (USPP) formalism[59]. We used an energy cutoff of 350 eV. Different Monkhorst-Pack k-point sets were used. The maximum self-consistent field convergent tolerance was less than 2×10^{-6} eV $atom^{-1}$. All calculations were performed in reciprocal space. For the surface energy calculation, the surface region is composed of a finite number of two-dimensional infinite planes formed by cutting the crystal along a particular Miller index (hkl) plane. In each plane, a two-dimensional cell represents every site in the plane. Following the approach of Tasker[60], several of these cells in successive planes comprise the basic repeat unit that contains the composition of the bulk crystal unit cell. The surface energy per unit area, $E^{hkl}_{surface}$, of a particular surface is calculated from the difference between the energy of the surface block, $E_{surface\ block}$, and the energy of the same number of bulk ions, E_{bulk}, per unit area, A (cross-sectional), thus

$$E^{hkl}_{surface} = \left(E_{surface\ block} - E_{bulk}\right)/A \quad (1)$$

For slab model construction, enough layers were used and the depths of the surface regions were chosen to be large enough to ensure full relaxation of the surface ions and convergence of the surface energy. In each of case, surface structures were fully relaxed until the total energy difference was converged within 0.001 eV.

1. Bruce, P. G., Freunberger, S. A., Hardwick, L. J. & Tarascon, J.-M. Li-O_2 and Li-S batteries with high energy storage. *Nat. Mater.* **11**, 19–29 (2012).
2. Girishkumar, G., McCloskey, B., Luntz, A., Swanson, S. & Wilcke, W. Lithium-air battery: promise and challenges. *J. Phys. Chem. Lett.* **1**, 2193–2203 (2010).
3. Christensen, J. *et al.* A critical review of Li/air batteries. *J. Electrochem. Soc.* **159**, R1–R30 (2011).
4. Li, F., Zhang, T. & Zhou, H. Challenges of non-aqueous Li-O_2 batteries: electrolytes, catalysts, and anodes. *Energy Environ. Sci.* **6**, 1125–1141 (2013).
5. Zhang, L. *et al.* High aspect ratio γ-MnOOH nanowires for high performance rechargeable nonaqueous lithium–oxygen batteries. *Chem. Commun.* **48**, 7598–7600 (2012).
6. Zhu, D., Zhang, L., Song, M., Wang, X. & Chen, Y. An in situ formed Pd nanolayer as a bifunctional catalyst for Li-air batteries in ambient or simulated air. *Chem. Commun.* **49**, 9573–9575 (2013).
7. Raghu, S. C., Ulaganathan, M., Aravindan, V. & Lim, T. M. Palladium- and Gold-Nanoparticle-Modified Porous Carbon as a High-Power Anode for Lithium-Ion Batteries. *ChemPhysChem* **14**, 3887–3890 (2013).

8. Lei, Y. *et al.* Synthesis of Porous Carbon Supported Palladium Nanoparticle Catalysts by Atomic Layer Deposition: Application for Rechargeable Lithium-O_2 Battery. *Nano Lett.* **13**, 4182–4189 (2013).
9. Cao, R. *et al.* Promotion of oxygen reduction by a bio-inspired tethered iron phthalocyanine carbon nanotube-based catalyst. *Nat. Commun.* **4**, 2076 (2013).
10. Hsieh, Y.-C. *et al.* Ordered bilayer ruthenium–platinum core-shell nanoparticles as carbon monoxide-tolerant fuel cell catalysts. *Nat. Commun.* **4**, 2466 (2013).
11. Laoire, C., Mukerjee, S., Plichta, E. J., Hendrickson, M. A. & Abraham, K. Rechargeable Lithium/TEGDME-$LiPF_6$/O_2 Battery. *J. Electrochem. Soc.* **158**, A302–A308 (2011).
12. Peng, Z., Freunberger, S. A., Chen, Y. & Bruce, P. G. A reversible and higher-rate Li-O_2 battery. *Science* **337**, 563–566 (2012).
13. Shui, J.-L., Karan, N. K., Balasubramanian, M., Li, S.-Y. & Liu, D.-J. Fe/N/C Composite in Li-O_2 Battery: Studies of Catalytic Structure and Activity toward Oxygen Evolution Reaction. *J. Am. Chem.Soc.* **134**, 16654–16661 (2012).
14. Li, F. *et al.* Carbon supported TiN nanoparticles: an efficient bifunctional catalyst for non-aqueous Li–O_2 batteries. *Chem. Commun.* **49**, 1175–1177 (2013).
15. Ryu, W.-H. *et al.* Bifunctional Composite Catalysts Using Co_3O_4 Nanofibers Immobilized on Nonoxidized Graphene Nanoflakes for High-Capacity and Long-Cycle Li-O_2 Batteries. *Nano Lett.* **13**, 4190–4197 (2013).
16. Yilmaz, E., Yogi, C., Yamanaka, K., Ohta, T. & Byon, H. R. Promoting Formation of Noncrystalline Li_2O_2 in the Li-O_2 Battery with RuO_2 Nanoparticles. *Nano Lett.* **13**, 4679–4684 (2013).
17. Zhong, L. *et al.* In Situ Transmission Electron Microscopy Observations of Electrochemical Oxidation of Li_2O_2. *Nano Lett.* **13**, 2209–2214 (2013).
18. Xu, J.-J., Wang, Z.-L., Xu, D., Zhang, L.-L. & Zhang, X.-B. Tailoring deposition and morphology of discharge products towards high-rate and long-life lithium-oxygen batteries. *Nat. Commun.* **4**, 2438 (2013).
19. Yang, H. G. *et al.* Anatase TiO_2 single crystals with a large percentage of reactive facets. *Nature* **453**, 638–641 (2008).
20. Mei Leng *et al.* Polyhedral 50-Facet Cu_2O Microcrystals Partially Enclosed by {311} High-Index Planes: Synthesis and Enhanced Catalytic CO Oxidation Activity. *J. Am. Chem. Soc.* **132**, 17084–17087 (2010).
21. Mou, X. *et al.* Rod-Shaped Fe_2O_3 as an Efficient Catalyst for the Selective Reduction of Nitrogen Oxide by Ammonia. *Angew. Chem. Int. Ed.* **51**, 2989–2993 (2012).
22. Xie, X., Li, Y., Liu, Z.-Q., Haruta, M. & Shen, W. Low-temperature oxidation of CO catalysed by Co_3O_4 nanorods. *Nature* **458**, 746–749 (2009).
23. Ji, Feng & Zeng, H. C. Size-Controlled Growth of Co_3O_4 Nanocubes. *Chem. Mater.* **15**, 2829–2835 (2003).
24. Rong Xu & Zeng, H. C. Mechanistic Investigation on Salt-Mediated Formation of Free-Standing Co_3O_4 Nanocubes at 95°C. *J. phys chem. B* **107**, 926–930 (2003).
25. Xiaowei Xie *et al.* Synthesis of Nanorod-Shaped Cobalt Hydroxycarbonate and Oxide with the Mediation of Ethylene Glycol. *J. Phys. Chem. C* **114**, 2116–2123 (2010).
26. Xu, R. & Zeng, H. C. Dimensional Control of Cobalt-hydroxide-carbonate Nanorods and Their Thermal Conversion to One-Dimensional Arrays of Co_3O_4 Nanoparticles. *J. Phys. Chem. B* **107**, 12643–12649 (2003).
27. Li, Y. *et al.* Iodine-ion-induced Size-tunable Co_3O_4 Nanowires and the Size-dependent Catalytic Performance for CO Oxidation. *ChemCatChem* **5**, 3576–3581 (2013).
28. Hou, Y. L., Kondoh, H., Shimojo, M., Kogure, T. & Ohta, T. High-yield preparation of uniform cobalt hydroxide and oxide nanoplatelets and their characterization. *J. Phys. Chem. B* **109**, 19094–19098 (2005).
29. He, T., Chen, D. R., Jiao, X. L. & Wang, Y. L. Co_3O_4 nanoboxes: Surfactant-templated fabrication and microstructure characterization. *Adv. Mater.* **18**, 1078–1082 (2006).
30. Yang, J., Liu, H., Martens, W. N. & Frost, R. L. Synthesis and Characterization of Cobalt Hydroxide, Cobalt Oxyhydroxide, and Cobalt Oxide Nanodiscs. *J. Phys. Chem. C* **114**, 111–119 (2010).
31. Zhao, Z., Geng, F., Bai, J. & Cheng, H.-M. Facile and controlled synthesis of 3D nanorods-based urchinlike and nonosheets-based flowerlike cobalt basic salt nanostructures. *J. Phys. Chem. C* **111**, 3848–3852 (2007).
32. Cao, A.-M. *et al.* Hierarchically structured cobalt oxide (Co_3O_4): The morphology control and its potential in sensors. *J. Phys. Chem. B* **110**, 15858–15863 (2006).
33. King, S., Hyunh, K. & Tannenbaum, R. Kinetics of nucleation, growth, and stabilization of cobalt oxide nanoclusters. *J. Phys. Chem. B* **107**, 12097–12104 (2003).
34. Feng, J. & Zeng, H. C. Size-Controlled Growth of Co_3O_4 Nanocubes. *Chem. Mater.* **15**, 2829–2835 (2003).
35. Chen, L., Hu, J., Richards, R., Prikhodko, S. & Kodambaka, S. Synthesis and surface activity of single-crystalline Co_3O_4 (111) holey nanosheets. *Nanoscale* **2**, 1657–1660 (2010).
36. Tang, X., Li, J. & Hao, J. Synthesis and characterization of spinel Co_3O_4 octahedra enclosed by the {111} facets. *Materials Research Bulletin* **43**, 2912–2918 (2008).
37. Petitto, S. C., Marsh, E. M., Carson, G. A. & Langell, M. A. Cobalt oxide surface chemistry: The interaction of CoO(100), Co_3O_4(110) and Co_3O_4(111) with oxygen and water. *Journal of Molecular Catalysis A: Chemical* **281**, 49–58, doi:10.1016/j.molcata.2007.08.023 (2008).
38. Linhua Hu, Qing Peng & Li, Y. Selective Synthesis of Co_3O_4 Nanocrystal with Different Shape and Crystal Plane Effect on Catalytic Property for Methane Combustion. *J. Am. Chem. Soc.* **130**, 16136–16137 (2008).
39. Wang, Y. *et al.* Crystal-match guided formation of single-crystal tricobalt tetraoxygen nanomesh as superior anode for electrochemical energy storage. *Energy Environ. Sci.* **4**, 1845–1854 (2011).
40. Zhou, Z.-Y., Tian, N., Li, J.-T., Broadwell, I. & Sun, S.-G. Nanomaterials of high surface energy with exceptional properties in catalysis and energy storage. *Chem. Soc. Rev.* **40**, 4167–4185 (2011).
41. Li, L. S. *et al.* Topotactic transformation of single-crystalline precursor discs into disc-like Bi_2S_3 nanorod networks. *Adv. Func. Mater.* **18**, 1194–1201 (2008).
42. Crossland, E. J. *et al.* Mesoporous TiO_2 single crystals delivering enhanced mobility and optoelectronic device performance. *Nature* **495**, 215–219 (2013).
43. Masaoki, Oku & Hirokawa, K. X-ray photoelectron spectroscopy of Co_3O_4, Fe_3O_4, Mn_3O_4, and related compounds. *J. Electron Spectrosc.* **8**, 475–481 (1976).
44. Charles, D. & Spencer, D. S. Mössbauer study of several cobalt spinels using Co57 and Fe57. *Phys. Rev. B* **9**, 3658–3665 (1974).
45. Prades, J. D., Cirera, A. & Morante, J. R. First-principles study of NO_x and SO_2 adsorption onto SnO_2 (110). *J. Electrochem. Soc.* **154**, H675–H680 (2007).
46. Tian, N., Zhou, Z. Y. & Sun, S. G. Platinum Metal Catalysts of High-Index Surfaces: From Single-Crystal Planes to Electrochemically Shape-Controlled Nanoparticles. *J. Phys. Chem. C* **112**, 19801–19817 (2008).
47. Tian, N., Zhou, Z. Y. & Sun, S. G. Electrochemical preparation of Pd nanorods with high-index facets. *Chem. Commun.* 1502–1504 (2009).
48. Han, X. G. *et al.* Controlling Morphologies and Tuning the Related Properties of Nano/Microstructured ZnO Crystallites. *J. Phys. Chem. C* **113**, 584–589 (2009).
49. Wang, Z. L. Zinc oxide nanostructures: growth, properties and applications. *J. Phys-Condens. Mat.* **16**, R829–R858 (2004).
50. Broqvist, P., Panas, I. & Persson, H. A DFT study on CO oxidation over Co_3O_4. *J. Catal.* **210**, 198–206 (2002).
51. Jansson, J. *et al.* On the Catalytic Activity of Co_3O_4 in Low-Temperature CO Oxidation. *J. Catal.* **211**, 387–397 (2002).
52. Lebedeva, N. P., Koper, M. T. M., Feliu, J. M. & van Santen, R. A. Role of crystalline defects in electrocatalysis: Mechanism and kinetics of CO adlayer oxidation on stepped platinum electrodes. *J. Phys. Chem. B* **106**, 12938–12947 (2002).
53. Zhang, D. Q. *et al.* Microwave-Induced Synthesis of Porous Single-Crystal-Like TiO_2 with Excellent Lithium Storage Properties. *Langmuir* **28**, 4543–4547 (2012).
54. Chen, J. S., Liu, H., Qiao, S. Z. & Lou, X. W. Carbon-supported ultra-thin anatase TiO_2 nanosheets for fast reversible lithium storage. *J. Mater. Chem.* **21**, 5687–5692 (2011).
55. Cui, L., Li, J. & Zhang, X.-G. Preparation and properties of Co_3O_4 nanorods as supercapacitor material. *J. Appl. Electrochem.* **39**, 1871–1876 (2009).
56. Amadon, B., Jollet, F. & Torrent, M. gamma and beta cerium: LDA + U calculations of ground-state parameters. *Phys. Rev. B* **77**, 155104(155101)–155104(155110) (2008).
57. Gonze, X. *et al.* ABINIT: First-principles approach to material and nanosystem properties. *Comput. Phys. Commun.* **180**, 2582–2615 (2009).
58. Gonze, X. *et al.* A brief introduction to the ABINIT software package. *Z Kristallogr* **220**, 558–562 (2005).
59. Perdew, J. P. & Wang, Y. Accurate and Simple Analytic Representation of the Electron-Gas Correlation-Energy. *Phys. Rev. B* **45**, 13244–13249 (1992).
60. Tasker, P. W. Stability of Ionic-Crystal Surfaces. *J. Phys. C Solid State* **12**, 4977–4984 (1979).

Acknowledgments

This original research was proudly supported by Commonwealth of Australia through the Automotive Australia 2020 Cooperative Research Centre (AutoCRC). The authors acknowledge use of facilities within the UOW Electron Microscopy Centre.

Author contributions

D.-W.S. performed the experiments. S.-X.D. and G.-X.W. conceived the study. D.-W.S. wrote the manuscript. All authors discussed the results on the manuscript and reviewed the manuscript. All authors revised the manuscript.

Additional information

Supplementary information accompanies this paper at http://www.nature.com/scientificreports

Competing financial interests: The authors declare no competing financial interests.

How to cite this article: Su, D.W., Dou, S.X. & Wang, G.X. Single Crystalline Co_3O_4 Nanocrystals Exposed with Different Crystal Planes for Li-O_2 Batteries. *Sci. Rep.* **4**, 5767; DOI:10.1038/srep05767 (2014).